Journal of Structural Biology 210 (2020) 107492

Contents lists available at ScienceDirect

Journal of Structural Biology

journal homepage: www.elsevier.com/locate/yjsbi

Pathology of myelinated axons in the PLP-deficient mouse model of spastic paraplegia type 2 revealed by volume imaging using focused ion beam-scanning electron microscopy

Anna M. Steyer[a,b,c], Torben Ruhwedel[a,b], Christos Nardis[a,b,c], Hauke B. Werner[a], Klaus-Armin Nave[a], Wiebke Möbius[a,b,c,*]

[a] Department of Neurogenetics, Max Planck Institute of Experimental Medicine, 37075 Göttingen, Germany
[b] Electron Microscopy Core Unit, Max Planck Institute of Experimental Medicine, 37075 Göttingen, Germany
[c] Center Nanoscale Microscopy and Molecular Physiology of the Brain (CNMPB), Göttingen, Germany

ARTICLE INFO

Keywords:
Focused Ion Beam-Scanning Electron Microscopy (FIB-SEM)
High-pressure freezing
Spastic paraplegia type 2 (SPG2)
Plp$^{-/Y}$ mouse
Myelin
Axonal swellings
Central nervous system (CNS)

ABSTRACT

Advances in electron microscopy including improved imaging techniques and state-of-the-art detectors facilitate imaging of larger tissue volumes with electron microscopic resolution. In combination with genetic tools for the generation of mouse mutants this allows assessing the three-dimensional (3D) characteristics of pathological features in disease models. Here we revisited the axonal pathology in the central nervous system of a mouse model of spastic paraplegia type 2, the *Plp*$^{-/Y}$ mouse. Although PLP is a *bona fide* myelin protein, the major hallmark of the disease in both SPG2 patients and mouse models are axonal swellings comprising accumulations of numerous organelles including mitochondria, gradually leading to irreversible axonal loss. To assess the number and morphology of axonal mitochondria and the overall myelin preservation we evaluated two sample preparation techniques, chemical fixation or high-pressure freezing and freeze substitution, with respect to the objective of 3D visualization. Both methods allowed visualizing distribution and morphological details of axonal mitochondria. In *Plp*$^{-/Y}$ mice the number of mitochondria is 2-fold increased along the entire axonal length. Mitochondria are also found in the excessive organelle accumulations within axonal swellings. In addition, organelle accumulations were detected within the myelin sheath and the inner tongue. We find that 3D electron microscopy is required for a comprehensive understanding of the size, content and frequency of axonal swellings, the hallmarks of axonal pathology.

1. Introduction

Focused ion beam-scanning electron microscopy (FIB-SEM) has become one of the highly used methods in the life sciences for the three-dimensional visualization of ultrastructural details in a tissue of interest. These technical developments allowed us to explore complex structures in 3D such as the spindle pole of mouse oocytes (So et al., 2019) or the change of distribution of ribbon synapses at the hearing onset of mice (Michanski et al., 2019). Addressing the ultrastructure of glial cells in the nervous system and their interactions with neuronal axons, FIB-SEM has been utilized to study repair mechanisms in peripheral nerves after injury (Gomez-Sanchez et al., 2017), the evolution of ensheathing glia (Weil et al., 2018) and the emergence of pathological outfoldings of myelin in the central nervous system (Erwig et al., 2019).

A variety of protocols exists to visualize structures of interest by serial block face imaging in the scanning electron microscope (SEM) after chemical fixation. For contrasting, the heavy metals osmium tetroxide and uranyl acetate as well as other contrasting agents including thiocarbohydrazide and tannic acid are widely used. Cryo-immobilization followed by freeze substitution has also been used to prepare samples for this imaging mode, aiming at structural preservation as close as possible to native conditions. Both techniques are not without technical challenges and may cause artifacts, necessitating careful interpretation and analysis of data.

In the mammalian nervous system, myelin is among the most difficult to preserve cellular structures, a multilayered sheath comprising lipid-rich membrane bilayers that are spirally wrapped around a central axon (the “axon myelin unit”). Proteolipid protein (PLP), the protein encoded by the *PLP1/Plp1* gene, is the major protein of central nervous

* Corresponding author.
E-mail address: moebius@em.mpg.de (W. Möbius).

https://doi.org/10.1016/j.jsb.2020.107492
Received 6 September 2019; Received in revised form 28 February 2020; Accepted 6 March 2020
Available online 08 March 2020
1047-8477/ © 2020 The Authors. Published by Elsevier Inc. This is an open access article under the CC BY-NC-ND license (http://creativecommons.org/licenses/BY-NC-ND/4.0/).

system myelin (Jahn et al., 2009; Werner et al., 2013). Indeed, the function of oligodendrocytes in preserving the integrity of myelinated axons (Griffiths et al., 1998; Möbius et al., 2008) involves the oligodendroglial expression of the *Plp*-gene (Lüders et al., 2017). Point mutations, gene duplications and deletions of the human *PLP1* gene give rise to a spectrum of neurodevelopmental disorders (leukodystrophies), ranging from severe Pelizaeus Merzbacher disease (PMD, most frequently caused by duplication of the *PLP1* gene) to the comparatively milder spastic paraplegia type 2 (SPG2) (Cailloux et al., 2000; Saugier-Veber et al., 1994). The $Plp^{-/Y}$ mouse as a model for SPG2 develops deficits in axonal transport (Edgar et al., 2004) with accumulations of organelles and mitochondria trapped in large axonal swellings leading ultimately to neurodegeneration throughout the CNS with a particular severity in long axons of the spinal cord (Griffiths et al., 1998; Lüders et al., 2019). Probably owing to the lack of the adhesive properties of PLP (Bakhti et al., 2013; Möbius et al., 2008; Bizzozero et al., 2001), myelin in these mutants is characterized by instability which makes it even more prone to sample handling and fixation artifacts during the sample preparation for electron microscopic evaluation. In addition, an increased number of cytoplasmic channels through otherwise compacted myelin sheaths is observed in $Plp^{-/Y}$ mice (Rosenbluth et al., 2006; Möbius et al., 2016). This structural feature is best preserved by sample preparation applying high-pressure freezing and freeze substitution. We note that most of these pathological characteristics were first observed using traditional two-dimensional transmission electron microscopy (Edgar et al., 2004; Griffiths et al., 1998; Rosenbluth et al., 2006).

Understanding of the SPG2-like disease mechanism leading to axonal pathology in $Plp^{-/Y}$ mice has remained fragmentary. Aiming at improved assessment of the pathological consequences of PLP-deficiency we applied three-dimensional (3D) electron microscopy on optic nerve samples of $Plp^{-/Y}$ mice, which exhibit the same signs of pathology as found in the spinal cord of SPG2 patients. Here, we could reveal details of the content and number of the axonal swellings (also termed spheroids) (Klugmann et al., 1997; Griffiths et al., 1998; de Monasterio-Schrader et al., 2013). Axonal swellings indicate disturbed axonal transport (Edgar et al., 2004) of organelles including mitochondria (Saab et al., 2013; Yin et al., 2016). Therefore, we also addressed morphological alterations affecting axonal mitochondria in $Plp^{-/Y}$ mice. Since mitochondrial morphology is influenced by chemical fixation, we evaluated changes potentially caused by sample preparation, comparing chemically fixed samples with high-pressure frozen and freeze substituted samples. Our data suggest that for volume imaging of mitochondria both methods are suitable. Furthermore we show that 3D analysis of axon-myelin units in $Plp^{-/Y}$ mice reveals important details of the SPG2-like pathology such as differences in the composition of axonal swellings and organelle accumulations within the myelin compartment.

2. Material and methods

2.1. High-pressure freezing and freeze substitution

$Plp^{-/Y}$ mice (Klugmann et al., 1997) kept on a C57Bl/6N background and wild type littermates were sacrificed by cervical dislocation at postnatal day 75 (P75). The optic nerves were dissected, cut and high-pressure frozen (Weil et al., 2019) using 20% Polyvinylpyrrolidone (PVP) as a filler and the HPM100 high-pressure freezer (Leica, Vienna, Austria). An automatic freeze substitution unit (Leica, AFSII) was used to perform the freeze substitution. 0.1% tannic acid in acetone was incubated at −90° C for 100 h followed by three acetone rinses for 30 min each. 2% OsO_4, 0.1% uranyl acetate in acetone was used for contrasting the samples (7 h at −90 °C). The temperature was automatically raised to −20 °C within 14 h, kept there for 16 h and raised to 4 °C within 2.5 h. OsO_4 was removed by washing four times with acetone for 30 min. The nerves were then rinsed with acetone for 1 h at room temperature. The samples were incubated with increasing concentrations of resin (2:1, 1:1, 1:2) for 2 h each and left in 90% Durcupan over night without component D. The next day the samples were incubated with 100% Durcupan (all components) for 4.5 h and polymerized for 48 h at 60 °C.

2.2. Chemical fixation

Dissected samples were immersed in primary fixative (Karlsson-Schultz phosphate buffer: 109.5 mM $NaH_2PO_4{\cdot}H_2O$, 93.75 mM $Na_2HPO_4{\cdot}2H_2O$, 86.2 mM NaCl, 2.5% glutaraldehyde, 4% formaldehyde. Adjust the pH to 7.4 and filter) and processed with a modified OTO-protocol (Deerinck et al., 2010), as described previously (Weil et al., 2018). The samples were rinsed three times for 15 min with 0.1 M phosphate buffer at 4 °C. Samples were post-fixed for 3 h with 2% OsO_4 and 1.5% $K_3Fe(CN)_6$ at 4 °C and rinsed three times with H_2O for 15 min each at 4 °C. They were further contrasted with 1% thiocarbohydrazide 1 h at room temperature, followed by three times 15 min rinsing with water and 1.5 h incubation with 2% OsO_4. After several washes with H_2O the samples were *en bloc* stained with 2% uranyl acetate overnight at 4 °C. The next day the nerve samples were rinsed three times for 15 min with H_2O and dehydrated through a series of ascending concentrations of acetone for 15 min each (30%, 50%, 75%, 90%, 3× 100%). The samples were incubated with increasing concentrations of resin (2:1, 1:1, 1:2) for 2 h each and left in 90% Durcupan over night without component D. The next day the samples were incubated with 100% Durcupan (all components) for 4.5 h and polymerized for 48 h at 60 °C.

2.3. TEM imaging

Ultrathin sections of embedded optic nerve samples were cut using an ultramicrotome (RMC PowerTome PT-PC, Science Services, Munich, Germany) and a 35° diamond knife (Diatome, Biel, Switzerland). Sections were placed on 100 mesh hexagonal copper grids (Science Services) and imaged with a LEO912 electron microscope (Carl Zeiss Microscopy, Oberkochen, Germany) and an on-axis 2 k CCD camera (TRS, Moorenweis, Germany).

2.4. Sample mounting, FIB-SEM and data acquisition

Samples were trimmed using a 90° trimming knife (Diatome) and positioned on a SEM-stub using silver conductive resin (EPO-TEK 129-4). The surface was sputtered coated (Leica, ACE 600) with a layer of 10 nm gold and placed inside the FIB-SEM (Crossbeam 540, Zeiss). After exposing a cross- section through the region of interest with 15 nA ion current and polishing with 7 nA, a 400 nm deposition of platinum was done using a 3 nA current. The final dataset was acquired at 1.5 kV (600/1000 pA, ESB grid 450 V) 5 nm × 5 nm × 25 nm voxel size with a milling current of 1.5/3 nA.

2.5. Image analysis

All following steps were performed using the image processing package Fiji (Schindelin et al., 2012): The images were aligned using the SIFT algorithm, cropped and inverted. They were smoothed using a Gaussian blur (sigma 1) and a local contrast enhancement was applied (CLAHE: blocksize 127, histogram bins 256, maximum slope 1.5). The axons and the mitochondria were manually segmented in IMOD (Kremer et al., 1996). The axonal swellings were reconstructed using MIB (Belevich et al., 2016), IMOD and Imaris (Bitplane).

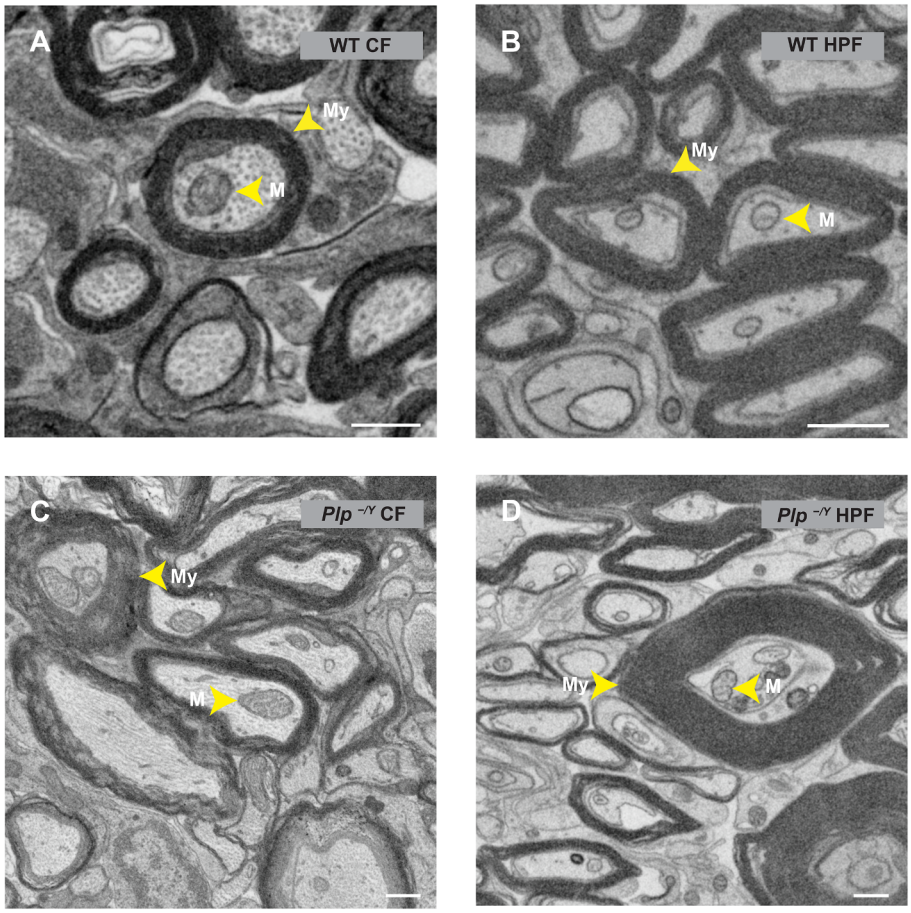

Fig. 1. Comparison of structural features in chemically fixed and high-pressure frozen optic nerves imaged by FIB-SEM. All images are extracted from FIB-SEM datasets. A) Chemically fixed axons in a WT optic nerve. B) High-pressure frozen axons in a WT optic nerve. Note that axonal microtubules are better visible in the chemically fixed sample. The overall structure of mitochondria is well visible in both preparations in this imaging mode. Fine details of the cristae structure are not resolved. C) Chemically fixed axons in *Plp*$^{-/Y}$ optic nerve. D) High-pressure frozen axons in optic nerve of a *Plp*$^{-/Y}$ mouse. Note that PLP-deficient myelin is prone to fixation artifacts; the compact myelin ultrastructure can be appreciated only in the HPF prepared sample. Arrow heads point to My = Myelin, M = Mitochondria. Scale bars, 500 nm.

3. Results

3.1. Image quality in high-pressure frozen and chemically fixed samples is sufficient for 3D data acquisition

First we addressed the question whether sample preparation by chemical fixation (CF) or high-pressure freezing (HPF) and freeze substitution (FS) provides samples suitable for volume imaging by FIB-SEM. We found that chemically fixed as well as high-pressure frozen samples exhibit sufficient contrast for FIB-SEM data acquisition (Fig. 1). In the HPF-prepared samples the contrast of microtubules was comparatively weak while in the chemically fixed samples axons were readily recognizable by the pattern of microtubule profiles (Fig. 1A and B). PLP-deficient myelin sheaths are instable and prone to fixation artifacts, probably because PLP is involved in the adhesion of adjacent myelin lamellae (Boison et al., 1995; Klugmann et al., 1997; Rosenbluth et al., 2006). In the datasets of the chemically fixed samples the lamella separation of the myelin sheaths was clearly visible and more pronounced (Fig. 1C), while in the high-pressure frozen dataset the overall appearance of the myelin was more consistent (Fig. 1D). On the other hand the interface between axon and myelin was better preserved in the chemically fixed samples. The occasionally observed separation of the axon and the myelin sheath in high-pressure frozen samples is probably due to distortions during handling of the fresh tissue and freezing (Fig. 1B and D). Taking these respective limitations into account, both sample preparations are useful for 3D data acquisition. Thus, FIB-SEM data stacks are a potential source of information about the shapes of organelles like mitochondria or the size, composition and distribution of organelle accumulations in axonal swellings.

For a careful assessment of the fine structural preservation a higher resolution by transmission electron microscopy was applied and provided more detail at the sub-organelle level, as exemplified by the membranes of axonal mitochondria (Fig. 2, coloured in blue). Mitochondrial cristae structure was differently preserved by the two sample preparation methods. In HPF prepared samples membranes appeared generally smoother. The inner and outer mitochondrial membranes are found in close apposition with a narrow intermembrane space. Also the contrast of cristae and lumen differed in the two sample preparation methods, probably due to unequal heavy metal staining (Fig. 2A and C compared to Fig. 2B and D). To be able to detect possible subtle pathological alterations of axonal mitochondria cristae morphology in *Plp*$^{-/Y}$ mice high TEM resolution preferentially by EM tomography is required. However, the same samples can be used for TEM, EM tomography and FIB-SEM. We conclude CF provides a better preservation of the axon-myelin interface and more contrast in axonal microtubules while HPF provides better preservation of myelin morphology. The overall mitochondrial structure with cristae is equally well visible in FIB-SEM images, but fine structural aspects of mitochondrial ultrastructure are preferentially studied with high-resolution TEM methods in HPF prepared samples.

3.2. Volumetric analysis reveals an increased number of axonal mitochondria in Plp$^{-/Y}$ *mice*

To investigate axonal mitochondria, optic nerves from *Plp*$^{-/Y}$ mice and littermate controls (n = 3) at the age of 75 days were chemically fixed or prepared by HPF and FS (n = 3) and respective 3D datasets covering a volume of about 15 µm × 15 µm × 20 µm (5 nm × 5 nm × 25 nm voxel size) were acquired. Per dataset five myelinated axons were segmented manually using IMOD (Kremer et al., 1996) including axons, myelin and mitochondria (Fig. 3, axonal membrane in yellow, axonal mitochondria in blue). In wildtype mice

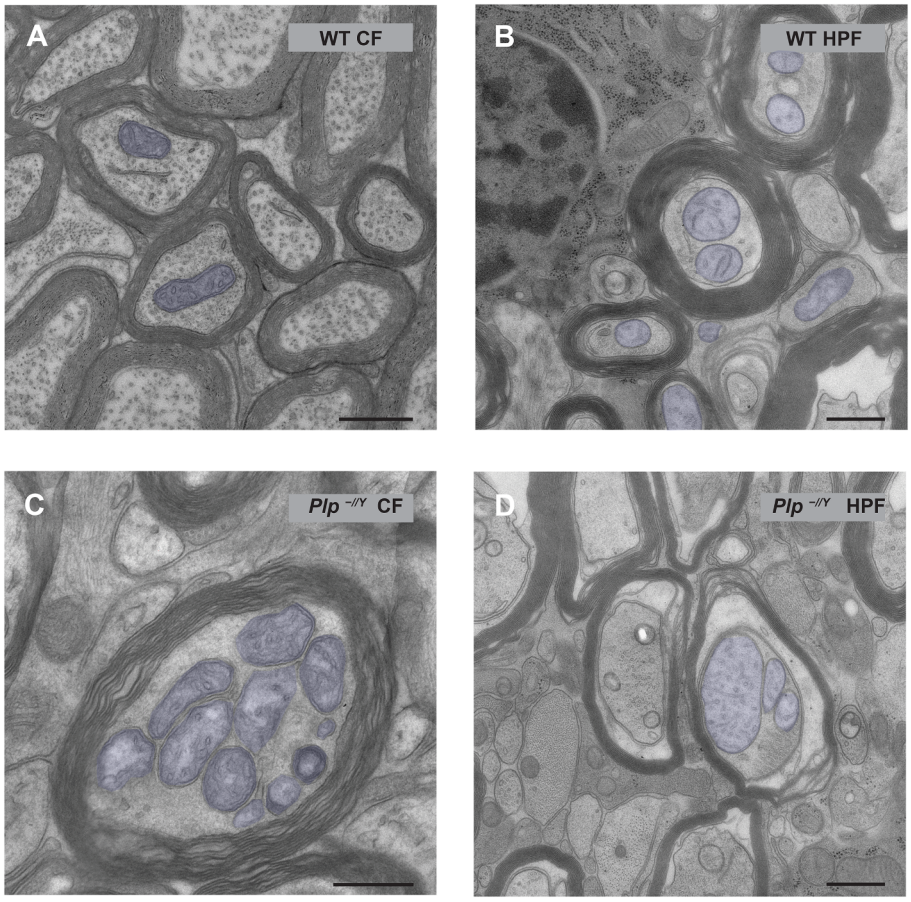

Fig. 2. Ultrastructure of axonal mitochondria by transmission electron microscopy of chemically fixed and high-pressure frozen optic nerves. Mitochondria are highlighted in blue. A) Axonal mitochondria in a chemically fixed WT optic nerve are characterized by a small diameter and rather dark contrast probably induced by the strong heavy metal staining applied to obtain sufficient contrast in the SEM. B) Mitochondria in a high-pressure frozen WT optic nerve. Note that the cristae structure is clearly visible. C) Mitochondria in a chemically fixed $Plp^{-/Y}$ optic nerve. D) Mitochondria in a high-pressure frozen optic nerve in $Plp^{-/Y}$. In both preparations mitochondria with abnormal morphology are detected when PLP is lacking. As in the WT samples, in the HPF prepared $Plp^{-/Y}$ samples the structure of the cristae is better preserved as judged by the narrow alignment of inner and outer membrane, the shape of the cristae and the smoothness of the membranes. This quality of preservation allows a judgement of distinct ultrastructural changes at the resolution of the TEM. Scale bars 500 nm.

the reconstructed axons displayed normally myelinated internodes with an average of 3 mitochondria per 10 μm axonal length (Fig. 3A and B and 4A). In comparison, $Plp^{-/Y}$ mice contained twice as many mitochondria per 10 μm myelinated axon (Fig. 3C and D and 4A). Axonal mitochondria in $Plp^{-/Y}$ mice appear shorter and rounder than those in wt animals, although the individual mitochondrial volume did not significantly differ between both genotypes (Fig. 4B) and, importantly, was not influenced by the sample preparation method (Fig. 4B). Taken together $Plp^{-/Y}$ mice display increased numbers of axonal mitochondria which are not enlarged, but show a different shape.

3.3. A minority of axonal swellings in the $Plp^{-/Y}$ mouse is enriched in mitochondria

Next we determined in FIB-SEM datasets to what extent mitochondrial accumulations contribute to axonal swellings which showed a remarkable diversity in size and content. For example, Fig. 5A illustrates a large axonal swelling containing mainly vesicular organelle accumulations and a few mitochondria. Other axonal swellings with a mixture of organelles are smaller (Fig. 5B), and yet other swellings contained largely mitochondrial accumulations (Fig. 5C, Supplementary movie 2). In 8 different FIB-SEM datasets 126 axonal swellings of different sizes (in 70000 μm^3 in total) were observed, sometimes in close vicinity to each other (Fig. 6E and Supplementary Table). This averages to one axonal swelling in a volume of 8.2 μm × 8.2 μm × 8.2 μm. From two of the $Plp^{-/Y}$ datasets (high-pressure frozen as well as chemically fixed) four axonal swellings were reconstructed in 3D. Two contained numerous mixed organelles (Fig. 6B/F and Supplementary movie 1), whereas the other two contained exclusively mitochondria (Fig. 6D). One of the reconstructed mitochondrial axonal swellings contained 170 mitochondria within 4.15 μm of axon length (Supplementary movie 2). From the 126 axonal swellings observed in total only 20 (16%) contained mainly mitochondria (Fig. 4C). We note that for a reliable detection of the mitochondrial content of the axonal swelling, the complete organelle accumulation has to be assessed, considering that several axonal swellings showed local heterogeneity within themselves which is typically not seen on thin sections. As an unexpected observation, we also detected organelle accumulations within the inner tongue as well as in myelinic channels of the myelin sheath. Notably, this feature can be easily overlooked and wrongly attributed to the axon. After revisiting the TEM sections, we found an example of accumulation in the inner tongue (Fig. 5D). In the 3D data stack, the localization of such an organelle cluster could be unequivocally assigned to the myelin compartment. In total we found 26 accumulations within the myelin inner tongue or myelinic channels in a volume of 70000 μm^3 averaging to one accumulation in a volume of 13.9 μm × 13.9 μm × 13.9 μm (Supplementary Table and Fig. 4C). This finding highlights aspects of myelin pathology contributing to the phenotype of the $Plp^{-/y}$ mouse.

Another interesting aspect to be addressed by volume EM is the localization of axonal swellings in relation to the myelin sheath and the node of Ranvier. In our datasets we found axonal swellings and organelle accumulations in unmyelinated axonal segments as well as in internodes. Interestingly, one of the reconstructed examples of an axonal swelling occurred in the non-myelinated section of the nodal area. We did not detect a local preference in the occurrence of swellings at specific sites of the axon, e.g. at the paranode. Since the imaged volume did not include complete internodes, a quantitative determination of the swelling distribution along internodes was not possible. Inside the swellings some elements are clearly recognizable as organelles, whereas in other areas the nature of the dense structures is not clearly discernible.

Taken together, 3D FIB-SEM analysis of the axon/myelin-units in $Plp^{-/Y}$ mice is possible on samples prepared by chemical fixation and

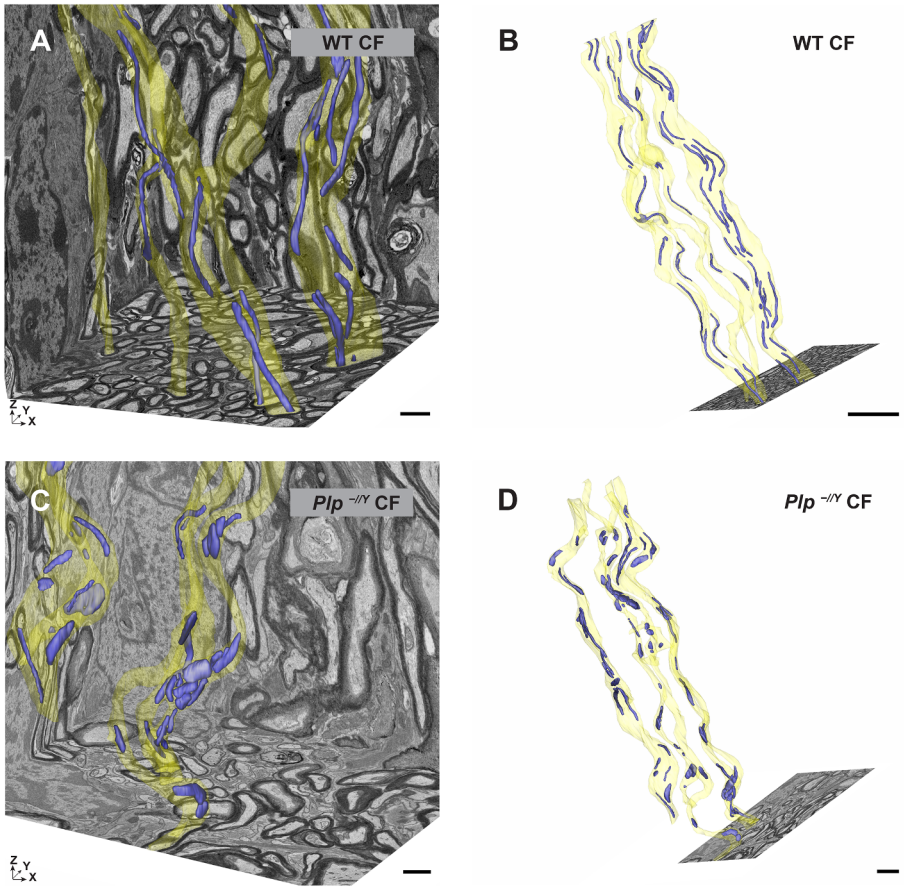

Fig. 3. 3-dimensional reconstruction of axons and their mitochondria in chemically fixed optic nerves. A/B) EM data resliced from FIB-SEM acquisition and 3D reconstruction of axons (yellow) and axonal mitochondria (blue) in chemically fixed optic nerves dissected from WT mice. Scale bar: A) 1 µm, B) 5 µm. C/D) EM data resliced from FIB-SEM acquisition and 3D reconstruction of axons (yellow) and mitochondria (blue) in chemically fixed $Plp^{-/Y}$ optic nerves. Axonal mitochondria in the WT optic nerve are more elongated and show a smaller diameter compared to the mitochondria in $Plp^{-/Y}$ optic nerve. In the mutant rounded mitochondria are more numerous. Scale bar C) 1 µm, D) 2 µm.

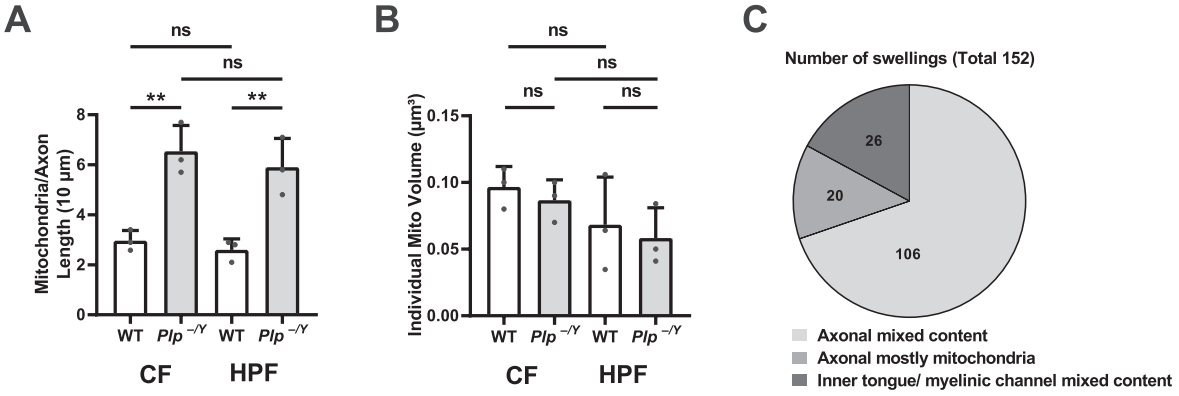

Fig. 4. Volumetric analysis of mitochondrial parameters in WT and $Plp^{-/Y}$. A) Number of mitochondria is increased in $Plp^{-/Y}$ compared to WT over an axonal length of 10 µm (n = 3 mice per genotype for CT and HPF) with 5 axons reconstructed per animal. CF: p = 0.0052 (**), HPF: p = 0.0098 (**), WT: p = 0.3579 (ns), $Plp^{-/Y}$: p = 0.5191 (ns). B) Volume of individual mitochondria, CF: p = 0.4676 (ns), HPF: p = 0.7067 (ns), WT: p = 0.2748 (ns), $Plp^{-/Y}$: p = 0.1471 (ns) Unpaired *t*-test. P < 0.05. Column, mean ± SD. The volume of the mitochondria is unaffected by the preparation method. C) Pie chart illustrates the different types of swellings. In total we found in 8 datasets (n = 6) 152 swellings which distribute to 126 axonal swellings of which 20 are mitochondrial enriched and 26 swellings located to the inner tongue/myelinic channels.

rOTO-embedding as well as by high-pressure freezing and freeze substitution as long as the general pathology is investigated rather than the fine ultrastructural details of myelin or mitochondria. For the latter EM tomography on HPF-prepared samples is the preferred method. Systematic acquisition and analysis of 3D data stacks provided a first quantitative assessment of the axonal pathology in this mouse model.

4. Discussion

Focused ion beam-scanning electron microscopy (FIB-SEM) allowed us to obtain 3D electron microscopic datasets of mouse optic nerves at high x/y/z resolution. It is a long standing standard that freezing, e.g. by high-pressure freezing, preserves the ultrastructure in a more native and less disturbed state compared to chemical fixation (Vanhecke et al., 2008). Any fine structural analysis therefore aims at imaging vitrified

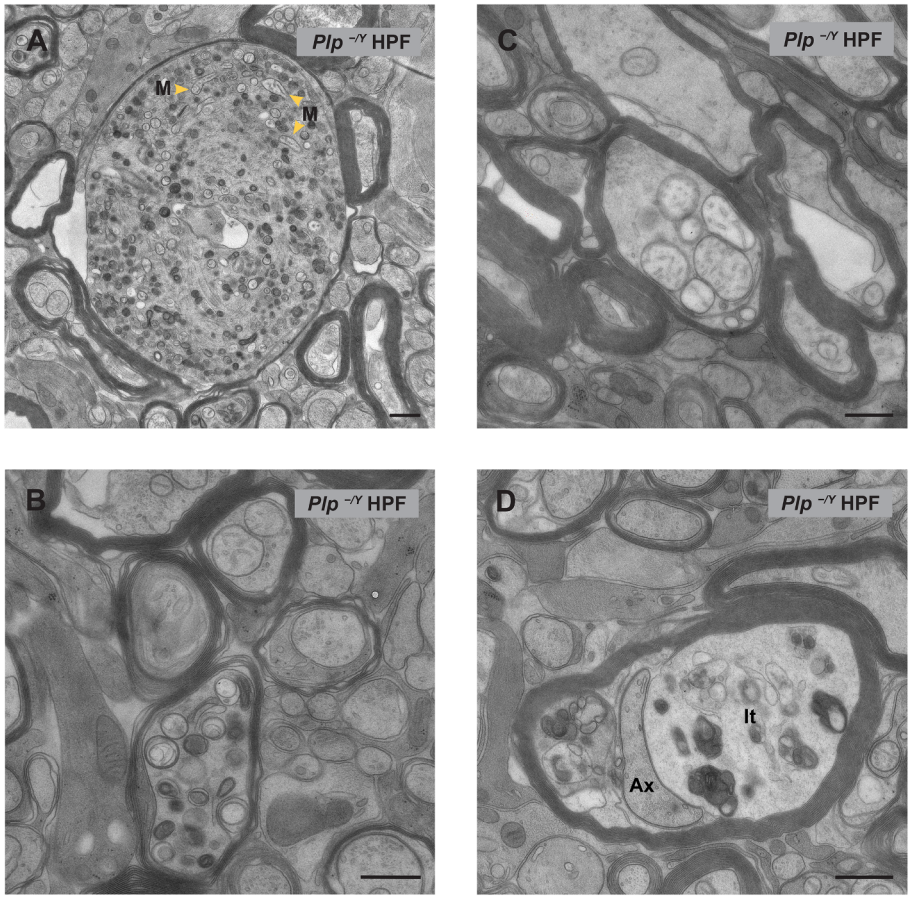

Fig. 5. TEM of organelle accumulations in the axon and inner tongue of the myelin sheath in high-pressure frozen optic nerves of *Plp*$^{-/Y}$ mice. A) Example of a large axonal swelling containing many organelles and also mitochondria (M = Mitochondria). B) Typical smaller sized axonal swelling with mixed organelle content. C) Axonal swelling composed of only mitochondria. D) An organelle accumulation in the inner tongue (It = inner tongue) of the myelin sheath (Ax = axon). Scale bars, 500 nm.

samples by cryo-electron microscopy (Koning et al., 2018). HPF and freeze substitution are regarded as the adequate approach for studying subcellular structure–function relationships in 3D (Noske et al., 2008). However, different preparation techniques can be used to prepare plastic-embedded samples for volume imaging by application of FIB-SEM. Depending on the particular question or the local availability of the technique one or the other method might be chosen. At higher resolution, transmission electron microscopy reveals that the membrane preservation is less disturbed after HPF and freeze substitution compared to chemically fixed samples, especially in the case of myelin (Möbius et al., 2010). Both sample preparation techniques may also be used for other 2D and 3D volume imaging techniques. For serial block-face scanning electron microscopy, more focus has previously been put on reducing charging of the sample, either by increasing the heavy metal content in the sample or by charge compensation in the instrument (Deerinck et al., 2018). TEM analyses and 3D electron microscopy by serial block-face imaging in the SEM were already applied for assessment of mitochondrial defects of chemically fixed rat brains (Eustaquio et al., 2018).

In the present study we show that samples prepared for high-resolution TEM analysis by HPF and freeze substitution were also suitable for acquiring FIB-SEM data stacks. Depending on the type of sample, the contrast generated by freeze substitution may not suffice. In such cases, additional contrasting steps may be included in the sample preparation protocol after completion of the freeze substitution (Hall et al., 2018; Steyer et al., 2019). High-pressure freezing combined with freeze substitution is thought to deliver more physiological results than chemical fixation if the tissue preparation is performed properly. This is of particular importance for studies in nervous tissue (Studer et al., 2014). In case of the mouse optic nerve, this white matter tract can be dissected freshly almost intact and fully functional. This tissue is therefore appropriate for preparation by HPF. For studying mitochondria HPF is also applied, since the inner mitochondrial membrane (Höhn et al., 2011) and the distribution of Ca^{2+} ions is well preserved (Kawahara et al., 2009). We therefore suggest that the findings in HFP-preserved optic nerve reflect the physiological conditions better than the chemically fixed samples and recommend avoiding chemical fixation for fine structural studies in mitochondria.

It is mechanistically not well understood how axonal integrity is impaired by the lack of PLP-expression from myelinating oligodendrocytes. The appearance of axonal swellings (Griffiths et al., 1998) and the increased number of axonal mitochondria (shown here) imply a metabolic imbalance in the axons resulting in a local energetic deficit, at least upon high-frequency axonal activity (Saab et al., 2013). Whether the axonal energy deficit is the direct cause of locally impaired motor driven transport or the cause of abnormal intra-axonal signalling cascades (and thus indirectly for the transport defect of mitochondria and other cargo) remains to be determined. Since we found that axonal swellings can be heterogeneous in composition along their length, large 3D data sets like those provided here are useful to gain insight into the dimensions and content of these organelle accumulations and how they are distributed along the internode.

We note that pathological changes affecting mitochondria were previously also observed by FIB-SEM in CNS axons of mice, in which myelin protein zero (MPZ/P0, the major constituent of peripheral nervous system myelin) was expressed in oligodendrocytes on a PLP-deficient background (Yin et al., 2016). This complex model shows accelerated axonopathy and shorter internodes compared to the *Plp*$^{-/Y}$ mouse (Yin et al., 2006), probably due to the targeted but aberrant incorporation of P0 into CNS myelin. In this model mitochondrial accumulations were preferentially detected in the juxtaparanodal segment and exhibited a shape change towards a more round morphology with a larger fraction of mitochondria with reduced cristae (Yin et al., 2016). In our SPG2-model we find a similar shape change towards a

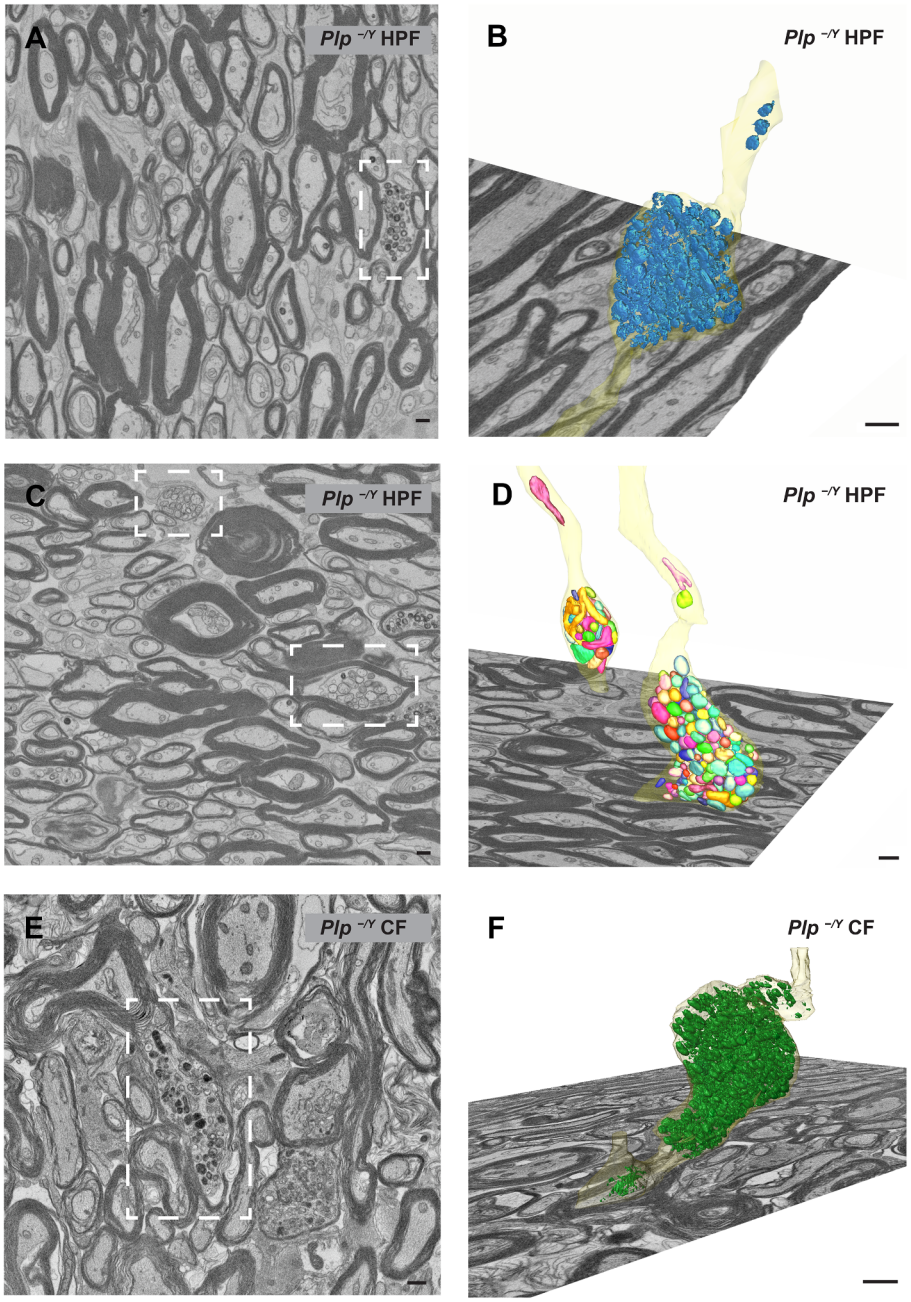

Fig. 6. 3D reconstruction of axonal swellings in optic nerves of *Plp*$^{-/Y}$ mice. A), C), E) Image from FIB-SEM data stack. B), D), F) 3D reconstruction of axonal swellings. A)–D) Data based on a high-pressure frozen sample. E)–F) Data based on a chemically fixed sample. A/B) and E/F) show axonal swellings which show mitochondria as well as other organelles and organelle-like structures (mixed content). C) and D) Two axonal swellings with the majority of the content being mitochondria (boxed areas in C). Scale bars 500 nm.

more round morphology, but a preferential localization of axonal swellings was not apparent.

Apart from the systematic assessment of the number and composition of axonal swellings and the shape and number of axonal mitochondria, we also found accumulations of organelles within the inner tongue of the myelin sheath. Such pathological features of the axon/myelin units in this mouse model of spastic paraplegia can only be detected and scrutinized by systematic application of 3D imaging by FIB-SEM. Further analysis for example by immunostaining is worthwhile to determine in more detail the content of these axonal swellings. Of special interest to deepen the understanding of the axonal pathology is the fine structure and functional state of the axonal mitochondria inside and outside of the swellings. Such a fine structure analysis requires higher resolution than FIB-SEM and should be performed by EM tomography on HPF-prepared samples.

CRediT authorship contribution statement

Anna M. Steyer: Conceptualization, Methodology, Investigation, Formal analysis, Writing - original draft. **Torben Ruhwedel:** Methodology, Investigation. **Christos Nardis:** Visualization, Data curation. **Hauke B. Werner:** Conceptualization, Resources, Writing - review & editing. **Klaus-Armin Nave:** Funding acquisition, Writing - review & editing. **Wiebke Möbius:** Supervision, Conceptualization, Funding acquisition, Writing - original draft.

Declaration of Competing Interest

The authors declare that they have no known competing financial interests or personal relationships that could have appeared to influence the work reported in this paper.

Acknowledgements

K.-A.N. holds a European Research Council (ERC) Advanced Grant (671048 'MyeliNano'). Part of this work (A.M.S. and C.N.) was supported by the Cluster of Excellence and DFG Research Center Nanoscale Microscopy and Molecular Physiology of the Brain. This work was also supported by the Deutsche Forschungsgemeinschaft (DFG) (MO 1084/2-1 (FOR2848) to W.M. and WE 2720/4-1 und WE 2720/2-2 to H.B.W).

Appendix A. Supplementary data

Supplementary data to this article can be found online at https://doi.org/10.1016/j.jsb.2020.107492.

References

Bakhti, M., Snaidero, N., Schneider, D., Aggarwal, S., Möbius, W., Janshoff, A., Eckhardt, M., Nave, K.-A., Simons, M., 2013. Loss of electrostatic cell-surface repulsion mediates myelin membrane adhesion and compaction in the central nervous system. Proc. Natl. Acad. Sci. 110, 3143–3148. https://doi.org/10.1073/pnas.1220104110.

Belevich, I., Joensuu, M., Kumar, D., Vihinen, H., Jokitalo, E., 2016. Microscopy image browser: a platform for segmentation and analysis of multidimensional datasets. PLoS Biol. 14, 1–13. https://doi.org/10.1371/journal.pbio.1002340.

Bizzozero, O.A., Bixler, H.A., Davis, J.D., Espinosa, A., Messier, A.M., 2001. Chemical deacylation reduces the adhesive properties of proteolipid protein and leads to decompaction of the myelin sheath. J. Neurochem. 76, 1129–1141. https://doi.org/10.1046/j.1471-4159.2001.00116.x.

Boison, D., Bussow, H., D'Urso, D., Muller, H.W., Stoffel, W., 1995. Adhesive properties of proteolipid protein are responsible for the compaction of CNS myelin sheaths. J. Neurosci. 15, 5502–5513. https://doi.org/10.1523/jneurosci.15-08-05502.1995.

Cailloux, F., Gauthier-Barichard, F., Mimault, C., Isabelle, V., Courtois, V., Giraud, G., Dastugue, B., Boespflug-Tanguy, O., 2000. Genotype–phenotype correlation in inherited brain myelination defects due to proteolipid protein gene mutations. Eur. J. Hum. Genet. 8, 837–845. https://doi.org/10.1038/sj.ejhg.5200537.

de Monasterio-Schrader, P., Patzig, J., Möbius, W., Barrette, B., Wagner, T.L., Kusch, K., Edgar, J.M., Brophy, P.J., Werner, H.B., 2013. Uncoupling of neuroinflammation from axonal degeneration in mice lacking the myelin protein tetraspanin-2. Glia 61, 1832–1847. https://doi.org/10.1002/glia.22561.

Deerinck, T.J., Bushong, E.A., Thor, A., Ellisman, M.H., 2010. NCMIR METHODS FOR 3D EM: A NEW PROTOCOL FOR PREPARATION OF BIOLOGICAL SPECIMENS FOR SERIAL BLOCKFACE SCANNING ELECTRON MICROSCOPY – SBEM Protocol v7_01_10.

Deerinck, T.J., Shone, T.M., Bushong, E.A., Ramachandra, R., Peltier, S.T., Ellisman, M.H., 2018. High-performance serial block-face SEM of nonconductive biological samples enabled by focal gas injection-based charge compensation. J. Microsc. 270, 142–149. https://doi.org/10.1111/jmi.12667.

Edgar, J.M., McLaughlin, M., Yool, D., Zhang, S.-C., Fowler, J.H., Montague, P., Barrie, J.A., McCulloch, M.C., Duncan, I.D., Garbern, J., Nave, K.A., Griffiths, I.R., 2004. Oligodendroglial modulation of fast axonal transport in a mouse model of hereditary spastic paraplegia. J. Cell Biol. 166, 121–131. https://doi.org/10.1083/jcb.200312012.

Erwig, M.S., Patzig, J., Steyer, A.M., Dibaj, P., Heilmann, M., Heilmann, I., Jung, R.B., Kusch, K., Möbius, W., Jahn, O., Nave, K.-A., Werner, H.B., 2019. Anillin facilitates septin assembly to prevent pathological outfoldings of central nervous system myelin. Elife 8. https://doi.org/10.7554/eLife.43888.

Eustaquio, T., Wang, C., Dugard, C.K., George, N.I., Liu, F., Slikker, W., Paule, M.G., Howard, P.C., Paredes, A.M., 2018. Electron microscopy techniques employed to explore mitochondrial defects in the developing rat brain following ketamine treatment. Exp. Cell Res. 373, 164–170. https://doi.org/10.1016/j.yexcr.2018.10.009.

Gomez-Sanchez, J.A., Pilch, K.S., Lans, M. Van Der, V, F.S., Benito, C., Wagstaff, L.J., Mirsky, R., Jessen, K.R., 2017. After nerve injury, lineage tracing shows that myelin and remak schwann cells elongate extensively and branch to form repair schwann cells, which shorten radically on remyelination 37, 9086–9099. https://doi.org/10.1523/JNEUROSCI.1453-17.2017.

Griffiths, I., Klugmann, M., Anderson, T., Yool, D., Thomson, C., Schwab, M.H., Schneider, A., Zimmermann, F., McCulloch, M., Nadon, N., Nave, K.A., 1998. Axonal swellings and degeneration in mice lacking the major proteolipid of myelin. Science (80-.) 280, 1610–1613. https://doi.org/10.1126/science.280.5369.1610.

Hall, T.J., Hartweig, E., Nguyen, K.C.Q., 2018. OTO Fixation for SEM and Blockface Imaging [WWW Document]. URL www.wormatlas.org/EMmethods/OTOFix.htm.

Höhn, K., Sailer, M., Wang, L., Lorenz, M., Schneider, E., Walther, P., 2011. Preparation of cryofixed cells for improved 3D ultrastructure with scanning transmission electron tomography. Histochem. Cell Biol. 135, 1–9. https://doi.org/10.1007/s00418-010-0765-z.

Jahn, O., Tenzer, S., Werner, H.B., 2009. Myelin proteomics: molecular anatomy of an insulating sheath. Mol. Neurobiol. 40, 55–72. https://doi.org/10.1007/s12035-009-8071-2.

Kawahara, I., Koide, M., Tadokoro, O., Udagawa, N., Nakamura, H., Takahashi, N., Ozawa, H., 2009. The relationship between calcium accumulation in osteoclast mitochondrial granules and bone resorption. Bone 45, 980–986. https://doi.org/10.1016/j.bone.2009.07.010.

Klugmann, M., Schwab, M.H., Schneider, A., Zimmermann, F., Griffiths, I.R., Nave, K., 1997. Assembly of CNS Myelin in the Absence of Proteolipid Protein 18, 59–70.

Koning, R.I., Koster, A.J., Sharp, T.H., 2018. Advances in cryo-electron tomography for biology and medicine. Ann. Anat. https://doi.org/10.1016/j.aanat.2018.02.004.

Kremer, J.R., Mastronarde, D.N., McIntosh, J.R., 1996. Computer visualization of three-dimensional image data using IMOD. J. Struct. Biol. 116, 71–76. https://doi.org/10.1006/jsbi.1996.0013.

Lüders, K.A., Nessler, S., Kusch, K., Patzig, J., Jung, R.B., Möbius, W., Nave, K.-A., Werner, H.B., 2019. Maintenance of high proteolipid protein level in adult central nervous system myelin is required to preserve the integrity of myelin and axons. Glia 67, 634–649. https://doi.org/10.1002/glia.23549.

Lüders, K.A., Patzig, J., Simons, M., Nave, K.-A., Werner, H.B., 2017. Genetic dissection of oligodendroglial and neuronal *Plp1* function in a novel mouse model of spastic paraplegia type 2. Glia 65, 1762–1776. https://doi.org/10.1002/glia.23193.

Michanski, S., Smaluch, K., Steyer, A.M., Chakrabarti, R., Setz, C., Oestreicher, D., Fischer, C., Möbius, W., Moser, T., Vogl, C., Wichmann, C., 2019. Mapping developmental maturation of inner hair cell ribbon synapses in the apical mouse cochlea. Proc. Natl. Acad. Sci. U. S. A. 201812029. https://doi.org/10.1073/pnas.1812029116.

Möbius, W., Cooper, B., Kaufmann, W.A., Imig, C., Ruhwedel, T., Snaidero, N., Saab, A.S., Varoqueaux, F., 2010. Electron Microscopy of the Mouse Central Nervous System. Methods Cell Biol. 96, 475–512. https://doi.org/10.1016/S0091-679X(10)96020-2.

Möbius, W., Nave, K.-A., Werner, H.B., 2016. Electron microscopy of myelin: Structure preservation by high-pressure freezing. Brain Res. 1641, 92–100. https://doi.org/10.1016/J.BRAINRES.2016.02.027.

Möbius, W., Patzig, J., Nave, K.-A., Werner, H.B., 2008. Phylogeny of proteolipid proteins: divergence, constraints, and the evolution of novel functions in myelination and neuroprotection. Neuron Glia Biol. 4, 111–127. https://doi.org/10.1017/S1740925X0900009X.

Noske, A.B., Costin, A.J., Morgan, G.P., Marsh, B.J., 2008. Expedited approaches to whole cell electron tomography and organelle mark-up in situ in high-pressure frozen pancreatic islets. J. Struct. Biol. 161, 298–313. https://doi.org/10.1016/j.jsb.2007.09.015.

Rosenbluth, J., Nave, K.A., Mierzwa, A., Schiff, R., 2006. Subtle myelin defects in PLP-null mice. Glia 54, 172–182. https://doi.org/10.1002/glia.20370.

Saab, A.S., Tzvetanova, I.D., Nave, K.-A., 2013. The role of myelin and oligodendrocytes in axonal energy metabolism. Curr. Opin. Neurobiol. 23, 1065–1072. https://doi.org/10.1016/J.CONB.2013.09.008.

Saugier-Veber, P., Munnich, A., Bonneau, D., Rozet, J.-M., Le Merrer, M., Gil, R., Boespflug-Tanguy, O., 1994. X–linked spastic paraplegia and Pelizaeus-Merzbacher disease are allelic disorders at the proteolipid protein locus. Nat. Genet. 6, 257–262. https://doi.org/10.1038/ng0394-257.

Schindelin, J., Arganda-Carreras, I., Frise, E., Kaynig, V., Longair, M., Pietzsch, T., Preibisch, S., Rueden, C., Saalfeld, S., Schmid, B., Tinevez, J.-Y., White, D.J., Hartenstein, V., Eliceiri, K., Tomancak, P., Cardona, A., 2012. Fiji: an open-source platform for biological-image analysis. Nat. Methods 9, 676–682. https://doi.org/10.1038/nmeth.2019.

So, C., Seres, K.B., Steyer, A.M., Mönnich, E., Clift, D., Pejkovska, A., Möbius, W., Schuh, M., 2019. A liquid-like spindle domain promotes acentrosomal spindle assembly in mammalian oocytes. Science 364, eaat9557. https://doi.org/10.1126/science.aat9557.

Steyer, A.M., Ruhwedel, T., Möbius, W., 2019. Biological sample preparation by high-pressure freezing, microwave-assisted contrast enhancement, and minimal resin embedding for volume imaging. J. Vis. Exp. e59156. https://doi.org/10.3791/59156.

Studer, D., Zhao, S., Chai, X., Jonas, P., Graber, W., Nestel, S., Frotscher, M., 2014. Capture of activity-induced ultrastructural changes at synapses by high-pressure freezing of brain tissue. Nat. Protoc. 9, 1480–1495. https://doi.org/10.1038/nprot.2014.099.

Vanhecke, D., Graber, W., Studer, D., 2008. Chapter 9: Close-to-Native ultrastructural preservation by high pressure freezing. Methods Cell Biol. 88, 151–164 https://doi.org/10.1016/S0091-679X(08)00409-3.

Weil, M.-T., Heibeck, S., Töpperwien, M., Tom Dieck, S., Ruhwedel, T., Salditt, T., Rodicio, M.C., Morgan, J.R., Nave, K.-A., Möbius, W., Werner, H.B., 2018. Axonal ensheathment in the nervous system of lamprey: implications for the evolution of Myelinating Glia. J. Neurosci. 38, 6586–6596. https://doi.org/10.1523/JNEUROSCI.1034-18.2018.

Weil, M.-T., Ruhwedel, T., Meschkat, M., Sadowski, B., Möbius, W., 2019. Transmission Electron Microscopy of Oligodendrocytes and Myelin. Humana Press, New York, NY, pp. 343–375.

Werner, H.B., Krämer-Albers, E.-M., Strenzke, N., Saher, G., Tenzer, S., Ohno-Iwashita, Y., De Monasterio-Schrader, P., Möbius, W., Moser, T., Griffiths, I.R., Nave, K.-A., 2013. A critical role for the cholesterol-associated proteolipids PLP and M6B in myelination of the central nervous system. Glia 61, 567–586. https://doi.org/10.1002/glia.22456.

Yin, X., Baek, R.C., Kirschner, D.A., Peterson, A., Fujii, Y., Nave, K.-A., Macklin, W.B., Trapp, B.D., 2006. Evolution of a neuroprotective function of central nervous system myelin. J. Cell Biol. 172, 469–478. https://doi.org/10.1083/JCB.200509174.

Yin, X., Kidd, G.J., Ohno, N., Perkins, G.A., Ellisman, M.H., Bastian, C., Brunet, S., Baltan, S., Trapp, B.D., 2016. Proteolipid protein-deficient myelin promotes axonal mitochondrial dysfunction via altered metabolic coupling. J. Cell Biol. 215, 531–542. https://doi.org/10.1083/jcb.201607099.